Science Advances

AAAS

advances.sciencemag.org/cgi/content/full/4/1/e1601453/DC1

Supplementary Materials for

Membrane insertion of—and membrane potential sensing by—semiconductor voltage nanosensors: Feasibility demonstration

Kyoungwon Park, Yung Kuo, Volodymyr Shvadchak, Antonino Ingargiola, Xinghong Dai, Lawrence Hsiung, Wookyeom Kim, Hong Zhou, Peng Zou, Alex J. Levine, Jack Li, Shimon Weiss

Published 12 January 2018, *Sci. Adv.* **4**, e1601453 (2018)
DOI: 10.1126/sciadv.1601453

The PDF file includes:

- table S1. Absorption anisotropy of NRs in the membrane.
- Reference (*56*)

Other Supplementary Material for this manuscript includes the following:
(available at advances.sciencemag.org/cgi/content/full/4/1/e1601453/DC1)

- movie S1 (.avi format). Fluorescence movie of pcNR-stained HEK293 cells.

section S1. Design of the peptide sequence for coating NRs

Selective insertion of peptide-coated nanorods (pcNRs) into membrane in a vertical orientation could be achieved by lipophilic coating of the central part of pcNRs and hydrophilic coating of the edges (Fig. 1). Edges and sides of pcNRs have the same chemical properties but different curvature of the surface. To selectively modified them, we decided to use a peptide containing α-helical and unstructured domains. Relatively rigid α-helical domain can bind cylindrical sides of NR but its binding to bended edges is less efficient, meanwhile the flexible part can efficiently fit curved surface of NR edges. The average size of NR is approximately 5 nm × 10 nm. We decided to construct a ~5 nm long peptide (half of the NR height) with strong gradient of polarity from the N- to C-terminus (Fig. 1B). Flexible polar C-terminal part is expected to bind edge of NR and determine peptide orientation. Lipophilicity of amino-acids gradually increases towards the N-terminus that is additionally modified by highly lipophilic myristoyl fatty acid residue that is expected to be located approximately at the center of NR. Affinity of the peptide to NR was achieved by introducing cysteines approximately at every third or fourth residue (Fig. 1D). In α-helical domain cysteines were located on one face of the helix (Fig. 1E). We also introduced two charged residues in the helical domain to avoid peptide aggregation and two residues having preferential positioning on membrane-water interface between α-helical and flexible parts of peptide to improve membrane localization.

section S2. Circular dichroism of the designed peptide

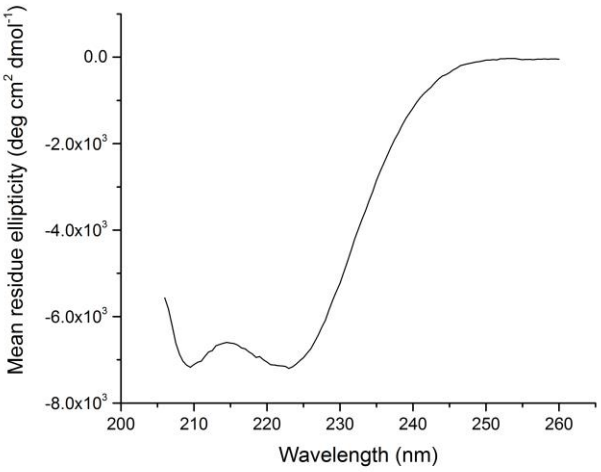

fig. S1. Circular dichroism spectrum of designed peptides dissolved in octanol.

The secondary structure of the designed peptides is determined by circular dichroism (CD). The peptides were dissolved in octanol, which mimics the nonpolar interior of the cell membrane. 4 mg of the peptides were dissolved in 1 ml of octanol and the excess solid peptides were filtered out to yield a saturated peptide solution. The concentration of the saturated peptide solution was determined to be ~17 μM (~0.05 mg/ml), by the absorbance of tryptophan at 280 nm using UV-Vis spectrometer. The CD spectrum was acquired at 25℃ under N_2 purge, using a quartz cuvette with 1 cm path length. The large, 1 cm path length was selected, due to the low solubility of the peptide in octanol and hence low absorbance of the solution when using a cuvette with 1 mm path length. The CD spectrum above 205 nm showed a characteristic alpha-helical structure, while the spectrum below 205 nm was oversaturated due to the solvent. (fig. S1).

section S3. Fluorescence anisotropy of pcNR-loaded vesicles

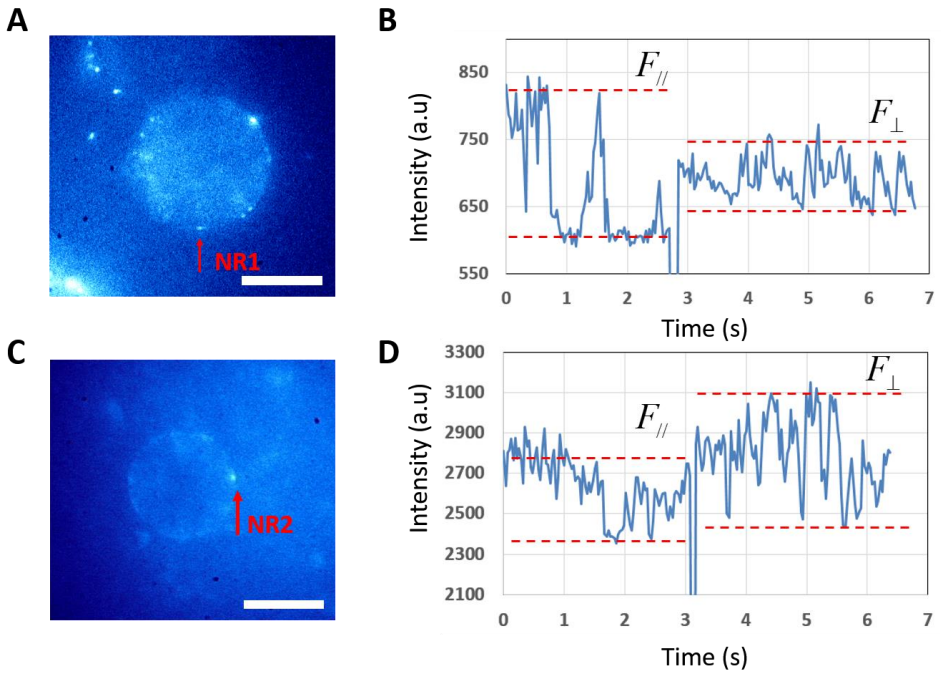

fig. S2. Orientation-dependent AA of pcNRs in membranes of GV. (**A**, **C**) fluorescence images of pcNR-loaded vesicles. NR1's (**B**) and NR2's (**D**) fluorescence trajectories, marked with red arrows in (A) and (C). During the measurement, the half-wave plate was removed, leading to excitation polarization change from vertical ($F_{//}$) to horizontal ($F_{\perp}$). Scale bar is 20 μm. An integration time is 32 ms.

To estimate pcNRs' orientation in membranes, we first made and attached vesicles to the microscopy cover glass. 8 μl (25 mM in chloroform) of 1,2-stearoyl-3-trimethylammonium-propane (DOTAP) and 1μl (25 mM in chloroform) of 1,2-dioleoyl-*sn*-glycero-3-phosphoethanolamine (DOPE) were mixed and dried under ambient condition. 100 μl of 100 mM NaCl with 1 volume percent of glycerol of distilled H_2O (dH_2O) were then added to the dried lipids, and stored in a 4ºC refrigerator for 24 hrs, followed by one minute of sonication. 5 μl of the vesicle solution was then loaded to the cover glass. To immobilize the vesicles, 500 μl of 100 mM NaCl in dH_2O (no glycerol) were added to the vesicle solution. After 10 minutes, immobilized giant vesicles (GV) could be observed. Finally, pcNRs were added to the vesicle-containing water droplet. Figure S2A and C show fluorescence images of pcNRs loaded vesicles, excited with

vertically polarized light. 200 frames movies were acquired and time trajectories from individual pcNRs were analyzed. During the movie acquisition, the excitation polarization was rotated by 90^o by removing a half-wave plate in the excitation path.

pcNRs at 0°, 90°, 180°, 270° of the vesicles' cross-section (at horizontal or vertical plane) are selected and analyzed. The representative intensity trajectories from membrane inserted pcNRs during polarization modulation are shown in fig. S2A and B. From such trajectories, absorption anisotropy ($AA = \frac{FP_{//} - FP_{\perp}}{FP_{//} + FP_{\perp}}$) could be obtained by measuring fluorescence signal. 26 pcNRs were analyzed and 15 out of them show AA corresponding to vertical orientation in membrane (AA > 0 for pcNRs in the vertical plane of GUV) indicating a preference towards vertical insertion, consistent with cryoEM results.

table S1. Absorption anisotropy of NRs in the membrane.

	Vertical plane	Horizontal plane
AA expected for transmembrane NR insertion [a)]	0.63	-0.5
AA expected for NR oriented parallel to membrane surface	-0.5	0.63
Average observed AA ±SD	0.12±0.30	-0.10±0.31
Number of pcNRs with transmembrane orientation [b)]	5	1
Number of analyzed pcNRs	17	9

[a)] Calculated based on the highest and lowest AA observed for all imaged pcNRs. The difference from 1 is because NR can be excited with light that is not in the plane of the main axis. The difference of the modules of values for vertical and horizontal plane are due to different intensity of the parallel and perpendicular light excitation.
[b)]including those with tilt less than 30° (the difference of AA from expected values was less than (1-cos30°)×100%)

section S4. Cell membrane staining with pcNRs

Fusogenic vesicles loaded with pcNRs was prepared as explained in Methods. They were added to cultured wild type HEK293 cells in PBS buffer. After incubating for 10 minutes, a series of confocal cross-sections was taken by Leica SP-2 microscopy. Figure S3 shows that the cell membranes are stained with pcNRs and pcQDs, respectively.

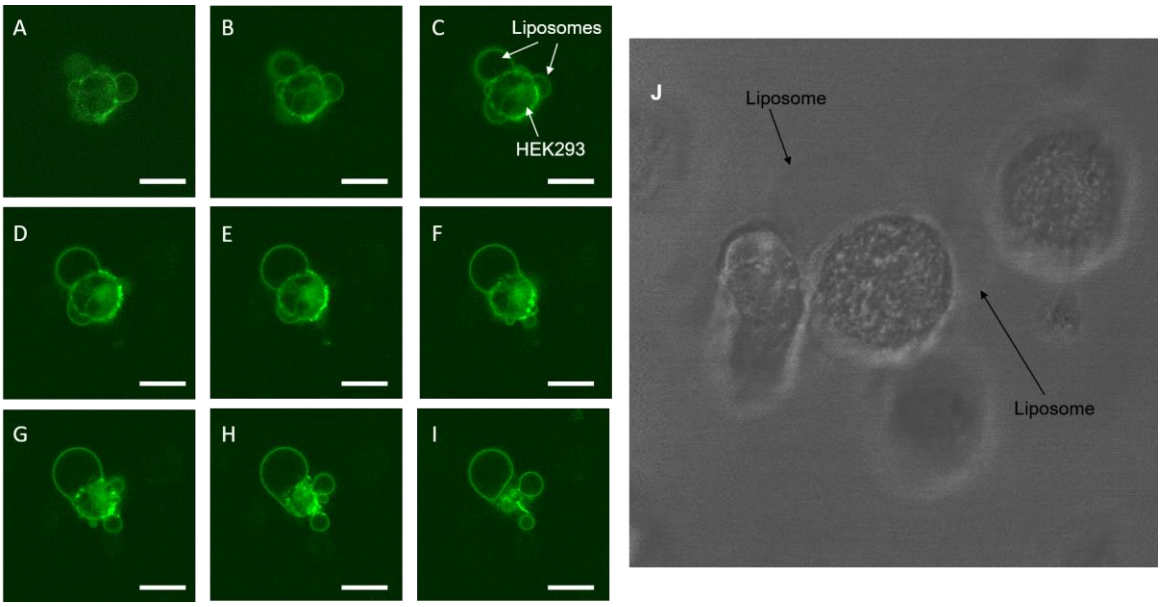

fig. S3. (A~I) Confocal cross-sections of an HEK293 cell fused with pcNR-loaded vesicles. Scale bar 10 μm. z-step is 0.5um. (**J**) A birth field image of (c) for clarifying the liposomes.

section S5. CryoEM control: Ligand-coated NRs do not insert into vesicles' membranes

As synthesized NRs were dissolved in toluene or hexane and precipitated by adding methanol multiple times to remove excess ligands. The NRs were then dissolved in DMSO and sonicated for 10 mins to minimize aggregation before adding to the vesicle solution (see Methods). 250 μl of the vesicle solution

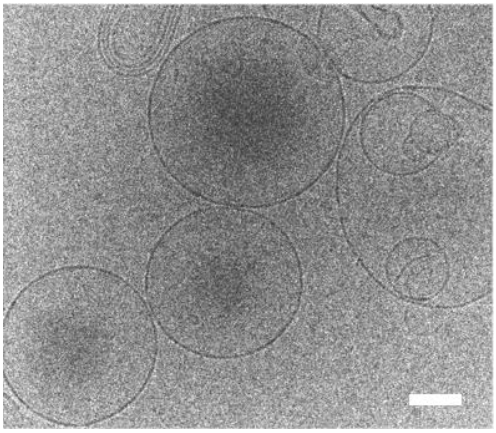

fig. S4. CryoEM images of vesicles after incubation with pcNRs. No NRs were observed to insert into the membrane. Scale bar 100nm.

was extruded through a membrane with 100 nm pore size to facilitate formation of 100 nm SUVs, and 2 μl of the NR solution in DMSO was mixed with the extruded vesicle solution. The mix solution was then deposited on TEM grids and frozen according to the methods described in Methods. As shown in fig. S4, the vesicles were not loaded with any NRs, indicating these NRs did not insert into the membrane of the vesicles.

section S6. Endocytosis of pcNRs after 1 hour of loading

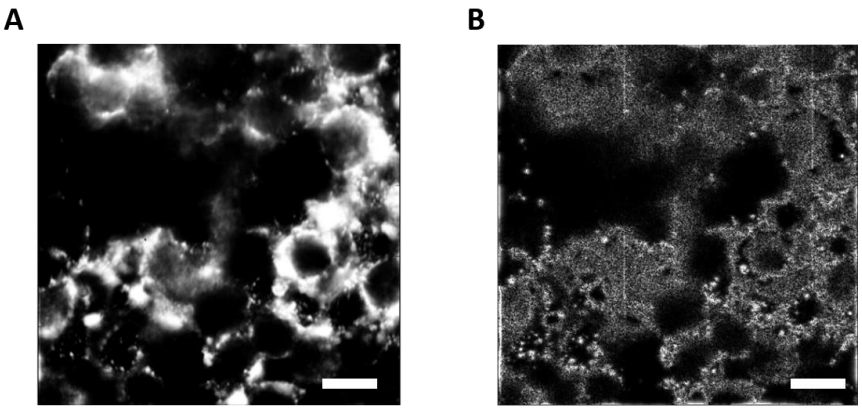

fig. S5. Images of pcNR-loaded HEK293 cells taken 1 hour later. (**A**) Fluorescence image of HEK293 cells after 1 hour of pcNRs' loading. (**B**) HPF filtered image. The same spatial filter in fig. S8 is used. Scale bar 10 μm.

section S7. Simulation of the energetics of the NR in the membrane

Since the energy of any nanorod configuration in the membrane is determined by the areas of hydrophobic and hydrophilic surfaces in contact with the interior of the membrane and (aqueous) solvent, the energy calculation becomes a straightforward exercise in geometry. In this section we outline calculation of the various areas involved in determining the nanorod insertion energy. We use these calculations to address two points. First, we examine the orientational stability of rods in the membrane by computing their mean tilt (or canting) angle with respect to the membrane local normal. We also consider the thermal fluctuations

of that tilting angle. Secondly, we consider the equilibrium partitioning of the nanorods between the solvent and the membranes, and find that for almost all hydrophobic (hydrophilic) energy scales and nanorod dimensions, the rods will strongly partition to the membrane.

SI-7.1 Geometry of the nanorod in the membrane

In the frame of the rod or radius a and length L, the points on the surface of the rod are given by

$$\tilde{\mathbf{r}} = a\cos\phi\hat{x}' + a\sin\phi\hat{y}' + \rho\hat{z}' \tag{7.1}$$

where $|r| < L/2$ and the azimuthal angle f covers the unit circle, $-p \pounds f < p$.

In the reference frame where the membrane (of thickness t) has unit normal $\hat{n} = \hat{z}$ and occupies the space $|z| < t/2$, the nanorod is oriented so that its symmetry axis lies along $\hat{p}$, $\hat{p} \times \hat{n} = \cos q$ and has its center at height h above the midplane of the membrane – see fig. S6A for a schematic representation of the configuration in terms of these degrees of freedom. Putting the nanorod in the xz-plane (without loss of generality) the surface of the cylinder lies on

$$\mathbf{r} = \hat{x}\left[r\sin q - a\cos q\cos f \right] + \hat{y}a\sin f + \hat{z}\left[h + r\cos q + a\sin q\cos f \right] \tag{7.2}$$

where ρ and f range over the same intervals as above. We neglect the endcaps of the cylinder for now.

The curve defining the intersection of the cylinder with the upper boundary of the membrane z = t/2 is given by

$$r_{top}^{(0)}\left(f\right) = \frac{t}{2\cos q} - \frac{h}{\cos q} - a\tan q\cos f \tag{7.3}$$

Since the ends of the cylinder may be in the interior of membrane, the upper limit of ρ is actually

$$r_{top}(f) = \min\left[\frac{L}{2}, r_{top}^{(0)}(f)\right] \tag{7.4}$$

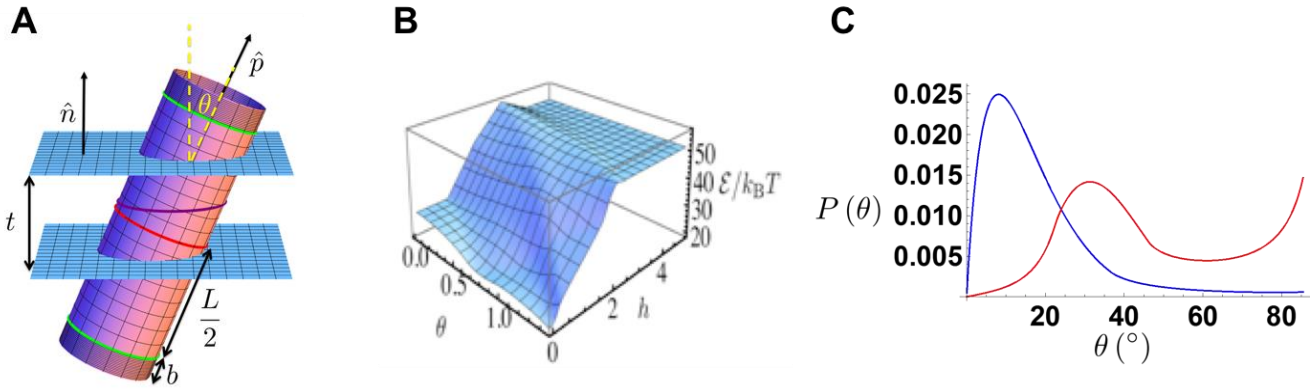

fig. S6. Canting angle distribution of NR. (**A**) Schematic of the nanorod in a membrane. hydrophobic length L with two hydrophilic ends of length b and radius a. The total length of the rod is then L + 2b. It is shown in a piece of membrane of thickness t. The green circles show the ends of the hydrophobic rod. The red circle denotes the center of the nanostructure, while the purple curve shows the intersection of the rod with the midplane of membrane. (**B**) Energy of the nanorod of radius a = 2 nm as a function of its orientation in the membrane, parameterized by , θ, h. The hydrophobic length of the rod is L = 8 nm, with hydrophilic end cylinders of length 2 nm. The energies (in units of k_BT/nm^2) are $\gamma_c^{\omega} = 2.0, \gamma_c^{o} = 0.1, \gamma_o^{\omega} = 0.1, \gamma_o^{o} = 1.0$. (**C**) Probability distribution for canting angle θ of a nanorod in the membrane for no hydrophobic mismatch L = t = 4 nm (blue) and significant hydrophobic mismatch L = 6 nm for the same membrane thickness. In both cases the rods are terminated at both ends by hydrophilic cylinders of length 2 nm.

For certain values of the vertical displacement h and tilt angle θ, the top of the cylinder is buried in the membrane, at least for some azimuthal angles f.

Similar considerations apply to the set of points on the cylinder where it intersects the lower edge of the membrane. These points are defined by

$$r_{bottom}^{(0)}(f) = -\frac{t}{2\cos q} - \frac{h}{\cos q} - a\tan q\cos f \tag{7.5}$$

As discussed with regard to Eq. 7.4, some of these points may be off the lower end of the cylinder when all or part of the bottom of the cylinder is buried in the membrane. To account for this case, we must use a lower limit given by

$$r_{bottom}(f) = \max\left[-\frac{L}{2}, r_{top}^{(0)}(f) \right] \tag{7.6}$$

To compute the surface area of the rod enclosed in the membrane, we integrate over the surface using the limits of integration obtained above in Eq. 7.4 and 7.6

$$A = \int_{p}^{p} a\, df \int_{r_{bottom}(f)}^{r_{top}(f)} dr\, \Theta(r;q,h,f) \tag{7.7}$$

where we include in the integrand Θ, which is vanishes if the bottom of the cylinder is above the upper edge of the membrane or if the top of the cylinder is below its lower edge.

The above analysis is designed to account for the central hydrophobic part of the cylinder, which is of length L. It is, however, a simple matter to compute the amount of hydrophilic surface area inside and outside the membrane by redoing the above analysis with different ranges of ρ. Specifically, to account for the upper hydrophilic part of the cylinder of length b, we shift the range of ρ to (L/2, L/2+b). The lower hydrophilic cylinder is corresponds to a range of ρ given by (-b-L/2, -L/2). The necessary adjustments to the min/max functions and to the Θ function are straightforward, but not given here.

SI-7.2 Energetics of the nanorod in the membrane

The energy of the nanorod is directly determined by four surface energies. We define $\gamma_c^{w,o}$ to be the surface energies, measured in units of k_BT/nm^2 of central hydrophobic rod in water (w) or in the oily (o) interior of the membrane $\gamma_c^o < \gamma_c^w$. We define two analogous surface energies for the outer hydrophilic parts of the rod, $\gamma_o^{w,o}$, where now $\gamma_o^w < \gamma_o^o$.

Height and orientational fluctuations of rods in the membrane

Because of the various geometrically required inequalities obeyed by the integration variables it is difficult to provide a generic, closed-form solution for the energy of the nanorod in the membrane $\varepsilon(\theta, h)$. Instead, we examine a specific case with L = 8 nm, a = 2 nm, b = 2 nm,

and a membrane of thickness t = 4 nm. In units of k_BT/nm^2, we take $\gamma_c^\omega = 2.0, \gamma_c^o = 0.1, \gamma_o^\omega = 0.1, \gamma_o^o = 1.0$. The energy surface is shown in fig. S6B.

There are two distinct features of this energy surface, both of which are attributable to the mismatch of the hydrophobic center to the membrane thickness. First, when we consider the potential along the h axis at a fixed canting angle θ, it is initially flat – small vertical displacements of nanorod do not change the energy as the hydrophobic section is longer than the width of the membrane. Once, the vertical displacement is sufficiently large so as to begin to bury the hydrophilic ends of the rod, the potential increases rapidly in a nearly linear fashion until the rod leaves the membrane entirely.

Second, when we consider the energy surface in the tilting (theta) direction near symmetric insertion (h = 0), we see that the hydrophobic mismatch between the central part of the rod and the membrane thickness leads to a decrease of energy with increasing angle. As the rod tilts, more hydrophobic surface is buried within the membrane lowering the total energy of the system. When the hydrophilic top or bottom of the rod touches the membrane, however, this energy reduction with increasing angle is arrested as it become energetically unfavorable to bury more and more of the hydrophilic ends inside the membrane. A local minimum in the energy appears at an angle which depends on the various surface energies of the two regions. We see then that the orientation of the rod along the local membrane normal is unstable to canting as a result of the hydrophobic mismatch. We will see below that, even in cases of zero hydrophobic mismatch, nonzero canting angles are still favored, now solely due to entropic considerations.

For the special case of zero hydrophobic mismatch, the rod is strongly pinned within the membrane, i.e., with h near zero. The effective potential for rod canting (i.e., angling with respect to the local membrane normal) is effectively linear in the angle $\sim a\theta$, with $a \sim O(10 k_B T)$ for typical values for nm scale rod dimensions and surface energies of a few $k_B T/nm^2$. Thus the mean canting angle of the rod is approximately given by

$$\langle \theta \rangle \approx -\partial_a \log\left[\int_0^\infty e^{-a\theta} \sin\theta\right] = \frac{2a}{1+a^2} \tag{7.8}$$

where, noting the rapid decay of the Boltzmann factor for larger angles, we have extended the upper limit of the integrand to infinity. As the potential is made steeper by, e.g., increasing the hydrophobic energy of the interior segment of the rod, the mean angle goes to zero as 2/a. This angle represents the competition between the energy cost for canting due to the burial in the membrane of the rod's hydrophilic ends and exposure of its hydrophobic interior to the surrounding solvent with the increased orientational phase space associated with larger canting angles.

The fluctuations about this mean value are given by

$$\langle \theta^2 \rangle - \langle \theta \rangle^2 \approx -\partial_a^2 \log\left[\int_0^\infty e^{-a\theta} \sin\theta\right] \approx \frac{2}{a^2} \tag{7.9}$$

in the region of interest. Thus, nanorods with no hydrophobic mismatch typically lie at small angles with respect to the membrane normal, $\langle \theta \rangle \sim 0.2 \sim 10^\circ$ and exhibit small fluctuations about this angle that are comparable to this angle: $\sqrt{\langle \theta^2 \rangle - \langle \theta \rangle^2} \sim \langle \theta \rangle$. Given the similar of the geometry of these nanorods to transmembrane proteins and their aggregates, we expect similar equilibrium orientations and fluctuations for them as well.

The key determinant of the canting angle distribution and the propensity for the nanorods to lie in the plane of the membrane $\theta \approx \pi/2$ appears to be the amount of hydrophobic mismatch – the difference in the thickness of the hydrophobic layer on the rod and the thickness of the membrane. In Fig. 2G (main text) we show the probability distribution for rod canting angles in the membrane for two rod geometries. In the first case (blue) the hydrophobic mismatch is zero; the length of hydrophobic section of the rod is equal to the membrane thickness L = t = 4 nm. Here we see a maximum in the angle probability distribution at angles comparable to the (small) mean canting angle $\langle\theta\rangle$ as computed from Eq. 7.8. In the second case (red), the hydrophobic section of the rod extends significantly beyond the boundaries of the membrane: L = 6 nm, while t = 4 nm. One observes that the local maximum in the probability distribution has moved to larger angles, with a maximum at a canting angle of $\theta \approx 0.6$, but there a new local maximum has developed for the case of the rod lying in the plane of the membrane, $\theta \approx \pi/2$. Sufficient hydrophobic mismatch will destabilize the (nearly) normal insertion orientation of the rods making them transmembrane poor voltage sensors. In both cases shown here (red and blue) the hydrophilic ends of the cylinder are 2nm long and all hydrophobic and hydrophilic surface energies are identical.

Partitioning of nanorod between solvent and membrane

To determine the equilibrium partitioning of nanorods between the membrane and surrounding fluid, we compare the partition function associated with a nanorod in aqueous solution of volume **V**

$$Z_{water} = 4\pi v \exp\left[-\left(4\pi ab\gamma_o^{\omega} + 2\pi aL\gamma_c^{\omega}\right)/k_B T\right] \tag{7.10}$$

with the partition function associated with the rod being in membrane of surface area **A**

$$Z_{membrane} = 4\pi A\int_0^{+1} d\cos(\theta)\int_{h_{\min}}^{h_{\max}} dh e^{-\varepsilon(\theta,h)/k_B T} \tag{7.11}$$

In Eq. 7.10 the prefactor of $4\pi V$ accounts for the orientational and translational degrees of freedom of the rod. These factors of are similarly accounted for in Eq. 7.11 by the prefactor of $2\times 2\pi A$. The first factor or two allows for the insertion of the rod in either of its two (identical) orientations. The remaining integrations in that equation are over the degrees of freedom determining the orientation of the rod in the membrane. The height integral is limited to $h_{min}(\theta)$ and $h_{max}(\theta)$ determined so that at least some part of the rod is in contact with the membrane.

We define the partitioning fraction of the nanorods R as the fraction of nanorods in the membrane of spherical vesicles of radius $\Re$ at number density n. From Eqs. 7.10, 7.11, this fraction is given by

$$R = \frac{r}{1+r} \tag{7.12}$$

where r is the ratio of the two partition sums given above: $r = Z_{membrane}/Z_{water}$. Taking these partition sums from Eqs. 7.10, 7.11, we find

$$r = 4\pi\Re^2 n \exp\left[\left(4\pi ab\gamma_o^{\omega} + 2paL\gamma_c^{\omega}\right)/k_BT\right]\int_0^{+1} d\cos(\theta)\int_{h_{\min}}^{h_{\max}} dh \exp\left[-\varepsilon(\theta,h)/k_BT\right] \tag{7.13}$$

The partitioning of the nanorods between the membrane and the solvent is controlled mainly by the hydrophobicity of the central part of the nanorod and the concentration of vesicles in solution. As long as these hydrophobic energies are significant, i.e., on the order of k_BT/nm^2 and the concentration of vesicles is at least in the nM (nanoMolar) regime, essentially all of the nanorods will be inserted into membranes in thermal equilibrium.

One may see this result from a simple estimate of the r factor defined in Eq. 7.13. To simplify the calculation, we assume that the energy difference between the rod in the membrane and in the (aqueous) solvent is due solely to the exposure of the hydrophobic surface of the nanorod to water

when in solution. Taking the length of the rod to be equal to the membrane thickness t, this Boltzmann weight associated with this energy difference is $\exp\left[2\pi at\gamma_c^{\omega}\right] \sim 10^{20}$. Taking there to be only $N \sim 10^9$ vesicles (of micron radius: $\Re = 1$ μm) per liter, we find the estimate for r to be

$$r \sim \frac{\Re^2 tNe^{2\pi at\gamma_c^{\omega}/k_B T}}{v} = 10^{14} \tag{7.14}$$

This estimate assumes that the excess energy cost of putting 1 nm^2 of hydrophobic surface in contact with water instead of the lipid membrane interior is 1 k_BT. Because of the exponential dependence of the result on this hydrophobic energy cost, reducing that energy difference to ~ 0.3 k_BT per nm^2, results in $r \sim O(1)$, implying a roughly equal partitioning of the nanorods between membrane and solvent, at least at this low membrane concentration.

section S8. Optical recording of ANEPPS-labeled and pcNR-labeled spiking HEK cells

ANEPPS stained membrane regions of HEK cells were thresholded (= mean + standard deviation). White pixels in fig. S7B are the area with intensity values that are larger than the threshold. Figure S7C shows a temporal time trajectory for the spatial average of all white pixels in fig. S7B, clearly exhibiting photo-bleaching. To remove this slowly varying contribution to the signal, we apply a 5th (M=5) order Butterworth-type high pass filter (HPF) with a cut-off frequency of f_c = 2.5 Hz

$$HPF_{time}(f) = \sqrt{1 - \left(\frac{1}{\sqrt{(1 + f / f_c)^{2M}}} \right)^2}$$

The blue curve in fig. S7D is the fast Fourier transform (FFT) of the signal shown in fig. S7C and the green curve represents the above mentioned Butterworth HPF. The red curve in fig. S7D

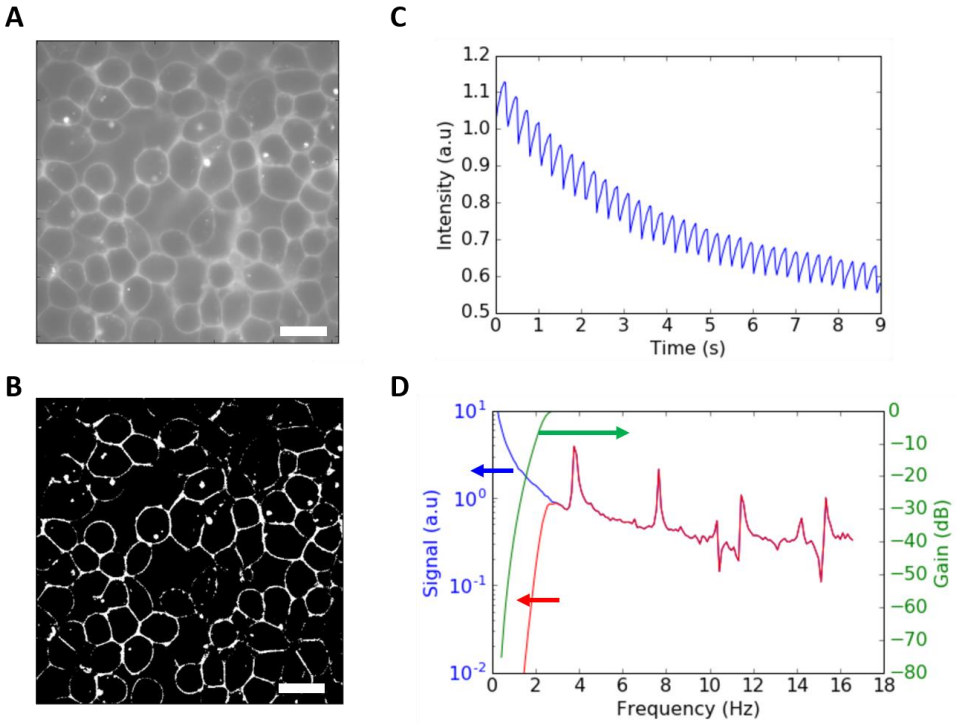

fig. S7. Image processing of voltage recording with ANEPPS. (**A**) Fluorescence image of ANEPPS stained spiking HEK293 cells (**B**) The binary image of (A) after thresholding. (**C**) Intensity time trace of white pixel's average in (B). (**D**) Blue: FFT of intensity time trace in (C). Green: The Butterworth temporal HPF function. Red: The filtered signal (frequency domain). Scale bar 10 μm.

represents the filtered signal (in the frequency domain). The black curve in Fig. 4D in time domain represents the filtered signal in the time domain.

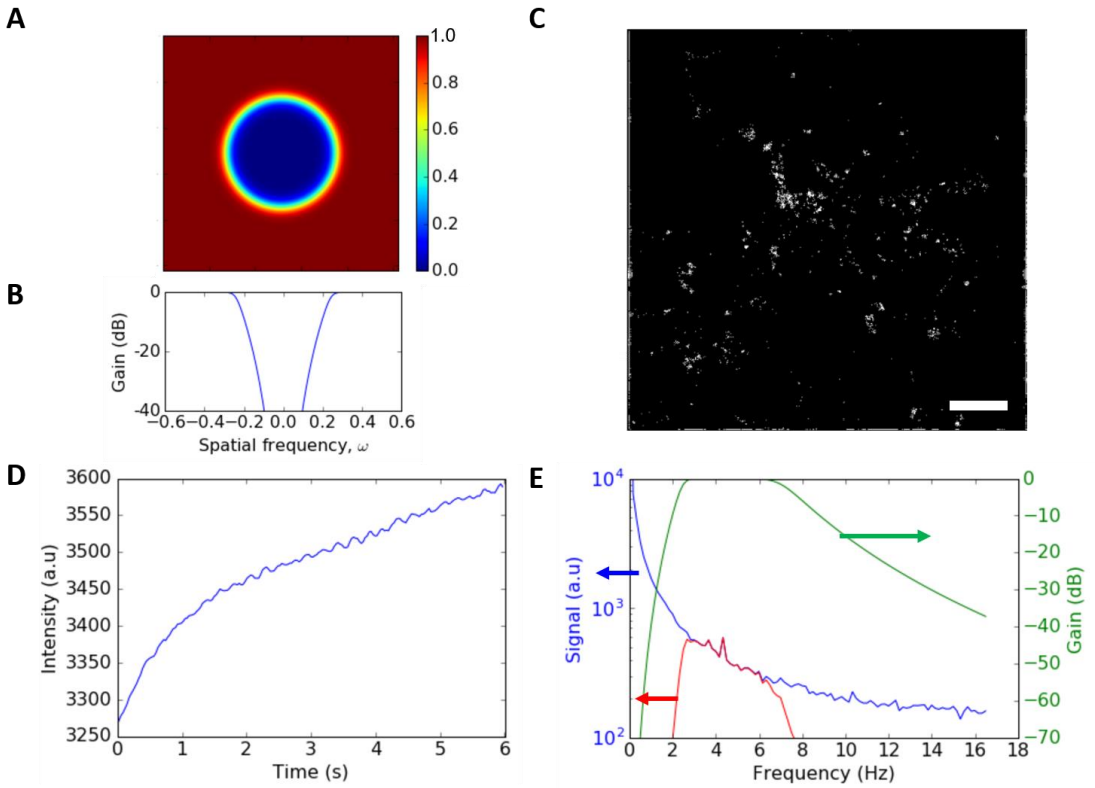

fig. S8. Image processing of voltage recording with pcNR. (**A**) A Butterworth type spatial HPF (**B**) The spatial HPF function at ω = 0. (**C**) The binary image of Fig. 4B after thresholding. (**D**) Intensity time trace of white pixel's average in (C). (**E**) Blue: FFT of intensity time trace in (D). Green: The temporal BPF function. Red: The BPF filtered signal. Scale bar 10 μm.

In contrast to the ANEPPS staining, staining with pcNRs is non-uniform, leading to local bright areas with gradients of brightness (The left side of Fig. 4B is brighter than the right side). We applied a 10th order high pass Butterworth filter with 0.244 (pixel^{-1}) as a spatial frequency (ω_c) cut-off. This filter removes the gradient and the cloudy background, increasing the visibility of single (or small aggregates) of pcNRs in Fig. 4C. Next, a simple threshold (= mean + 2 × standard deviation) is applied to obtain a binary image (fig. S8C). Using this binary image as a mask, we calculate the intensity time trance averaged over these white pixels (fig. S8D). Unlike the ANEPPS' result, the staining with pcNRs suffers from photo-brightening**.** To remove this slowly

varying contribution to the signal, and the high-frequency shot-noise, we apply a 5th (M=5) order of Butterworth band pass filter (BPF) with f_{low} = 2.5 Hz and f_{high} = 7 Hz as cut-off frequencies

$$BPF_{time}(f) = \frac{1}{\sqrt{(1+f/f_{high})^{2M}}}\sqrt{1-\left(\frac{1}{\sqrt{(1+f/f_{low})^{2M}}}\right)^2}$$

The blue curve in fig. S8E is the fast Fourier transform (FFT) of the temporal signal in fig. S8D and the green curve is the BPF function. The red curve in fig. S8E represents the filtered signal (frequency domain). The filtered signal in the time domain is shown in Fig. 4F, black curve.

The spiking cell analysis's data are freely available on figshare: https://figshare.com/articles/zqd_tif/4229531. The analysis code is published in a public github repository : https://github.com/pkw0818/spiking-cell-analysis.

section S9. Simultaneous optical and electrical recordings in patch-clamp experiment

SI-9.1 Data files and software

The data files used in the voltage sensing patch clamp experiment are freely available on figshare: http://dx.doi.org/10.6084/m9.figshare.1445980, dataset *122018_take1 100Hz.zip*. The dataset from the patch-clamp experiment consists of a video (272x192 pixels, 2000 frames at 400Hz or 2.5 ms per frame) and a synchronous set of electrical measurements (voltage, current) acquired by a DAQ interface at 10kHz.

Data analysis was performed in python using the Jupyter/IPython Notebook (*56*) and a few common scientific libraries (numpy, scipy, matplotlib, pandas). The Jupyter notebooks are "live" (i.e. re-executable) documents that contains both a narrative description of the analysis, the code commands and the output (figures, text, links, etc …). All the software used for data analysis of the patch-clamp experiment are open source and readily available on the internet.

The custom software used for patch-clamp data analysis is published in a public github repository: https://github.com/tritemio/voltagesensing where interested readers can find instructions on how to setup and reproduce the entire data analysis workflow. The repository contains a few .py files (python modules) containing low-level functions (data load, timetrace processing, burst search) and a set of Jupyter/IPython Notebooks that perform the full analysis. The notebook used in this paper can be also visualized online (read-only) at the following address: Patch Clamp Analysis - Phase offset-take1. Upon execution, the notebook generates an extensive set of plots of each analysis step and saves, in the *paper figures* folder, all the figures used in this publication (for the patch-clamp experiment). Finally, the raw unprocessed time-traces for each nanoparticle are saved in plain text format in the *results* folder in order to facilitate re-analysis with other tools.

SI-9.2 pcNR identification and ROIs

From the datatset linked above, we manually identified pcNRs positions with sub-pixel accuracy, by analyzing average frames on the raw video and on a temporal high-pass version of the video. The notebook in section 3 (link) contains figures of the center position of each identified pcNR for particles on the patched cell membrane (in the center of the field of view) and on unpatched cells' membranes. For brevity we will call these groups patched and unpatched pcNR.

A round ROI, centered on the pcNR position, is defined using a pixel radius of 1.8 pixels, resulting in a selection of roughly 20 pixels. Due to the pixel discretization and sub-pixel positioning of the pcNR the exact number of pixels selected for each particle can be slightly different. The notebook shows the exact ROI employed for each patched or unpatched pcNR (cells `In [38]` and `In [39]`).

SI-9.3 Time-trace extraction, filtering and blinking removal

For each identified pcNR, we compute the time-trace $\{t_k\}$ by averaging the signal in each ROI for each frame. Each of these raw time-traces is a 2000-element array, each element corresponding to a single video frame (the first 4 frames are discarded on loading since they systematically contain corrupted data due to specificities of the acquisition system). The voltage modulation has a period of 4 frames, of which the first 2 correspond to voltage-on and the last 2 to voltage-off semi-periods. Raw and processed timetraces are shown in the notebook section 4 (link).

In order to remove the time intervals where the pcNR is not fluorescent (due to blinking), a threshold is usually applied. In the present case, a slow-varying drift in the raw time-traces (1 s time scale) makes it difficult to identify a meaningful threshold. Therefore, we first apply a filter that removes the slow (low frequency) variations in the time-trace. This filter is a high-pass Gaussian filter with sigma of 300 frames (750 ms, see notebook figure `In[42]`). Next, we smooth the time-trace by applying a low-pass filter (Gaussian filter with sigma=10 frames, 25ms) in order to better identify the switch-points related to the particle fluorescence intermittency (blinking). Due to noise, without this smoothing step, we could erroneously detect multiple spurious ON/OFF transitions in correspondence with a single switch-point. Figures of the filtered time-traces overlaid with the smoothed version used to identify the blinking periods are shown in the notebook section 4 (figures `In[44]` and `In[45]`).

Finally, the dark-state periods are removed from each time-trace, making sure that a 4 frames alignment is preserved so that the reduced time-traces are still in phase with the alternation signal. This operation is performed by two python function: the function `get_on_periods_slices()` (link) performs the quantization to multiple of 4 frames for the start-stop index of each ON blinking

period; `get_on_periods_timetrace()` (link) performs the stitching of the ON blinking periods in the time-traces.

SI-9.4 Computing the modulated signal

Since each semi-period of the modulating voltage square-wave corresponds to 2 frames in $\{t_k\}$, we reduce the time-traces by averaging the array in blocks of 2 elements (implemented by `block_average()` in *timetraces.py*). The resulting reduced time-trace $\{\bar{t}_j\}$ has 1 element per semi-period (either ON or OFF voltage). Next, the "alternated differences" $\{\Delta F_i\}$ are computed as $\{(\bar{t}_1 - \bar{t}_0), -(\bar{t}_2 - \bar{t}_1), (\bar{t}_3 - \bar{t}_2), ...\}$ (the sign alternates and is "+" for ON-OFF and "-" OFF-ON transitions). This operation is implemented by `edge_diff_all()` in *timetraces.py*. Please note that one modulation period corresponds to 2 elements in the $\{\Delta F_i\}$ array.

The signal $\{\Delta F_i\}$, the normalized version $\{\Delta F_i / F\}$ (where *F* is the average time-trace value) and several derived statistics are computed both for particles in the patched cell membrane (*patched set*) and for particle in other position of the field of view (*unpatched set*).

As a control, an out-of-phase version of $\{\Delta F_i\}$ is computed by simply removing the first frame from the raw time-trace prior to the other processing steps. In this case, when computing the 2-element block average to obtain the reduced time-traces, the frame removal results in averaging one ON and one OFF semi-period frame. As a consequence, intensity variations due to the voltage modulations are suppressed. The distribution of out-of-phase $\{\Delta F_i\}$ values has a theoretical mean of zero and a standard deviation that is a characteristic of the background.

Histograms of the in-phase and out-of-phase signal distributions are reported in notebook section 8 (link). Several statistics for the alternated differences $\{\Delta F_i\}$ are reported in the notebook (i.e.

mean, standard deviation, mean/standard deviation, mean/(mean intensity)). Here, in fig. S9, we show the mean signal for different pcNRs. We note that among the patched pcNRs in positions #0, #1, #3, #4 and #8 exhibit significantly higher signal than the out-of-phase signal and the signals for unpatched particles. However, the pair of positions #0 - #1 (and #3 - #4), have pixels in common (i.e. the ROIs overlap) and show highly correlated time-traces, indicating that the signals are originated from the same particles (or small cluster of particles). In order to avoid treating those pairs as separate particles (and over-representing those positions which exhibit high signal), we discard positions #0 and #3 in the following analysis steps.

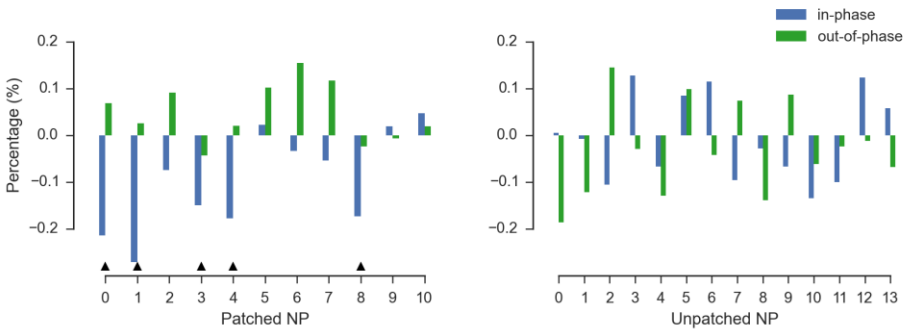

fig. S9. Mean of {$\Delta F_i/F$} for the two sets of patched (left) and unpatched (right) particles.

The patched particles #0, #1, #3, #4, and #8 (black marks) exhibit higher absolute in-phase signal than out-of-phase and unpatched particles.

Figure S10A and S10B show aggregated results for patched and unpatched NPs, both for in-phase and out-of-phase signal. In fig. S10A we show the full distribution for the 4 cases, whereas fig. S10B shows the distribution mean and the $\pm 1\sigma$ error range (computed under assumption of Gaussian distribution). We note that only the in-phase signal for the "patched" set exhibits a statistically significant deviation from 0. The full distribution shows also a larger negative tail for the patched in-phase signal suggesting that there may be a few temporally interspersed "bursts" of negative signal.

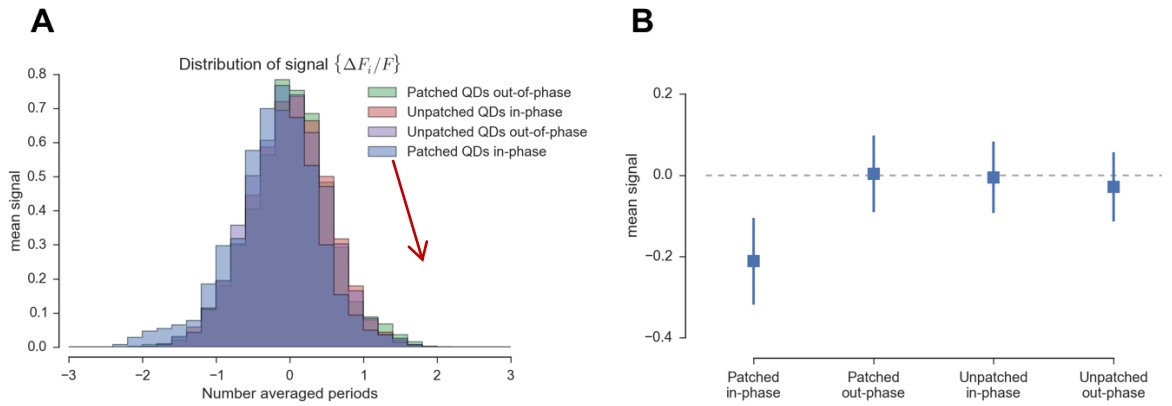

fig. S10. Image processing of voltage recording with pcNRs. (**A**) Distribution of signal $\{\Delta F_i/F\}$ aggregated from patched (only particles 1, 4 and 8) and unpatched particles, computed either in-phase or out-of-phase. The red arrow highlights the negative tail of the distribution that is more pronounced for the patched set with in-phase signal. (**B**) Mean signal $\{\Delta F_i/F\}$ aggregated from patched (only particles 1, 4 and 8) and unpatched particles, computed either in-phase or out-of-phase. The error bars correspond to the ±1σ range. Assuming a Gaussian distribution, σ is computed as $\sigma = \text{std.dev.}\left(\left\{\frac{\Delta F_i}{F}\right\}\right)/\sqrt{N}$, where *N* is the number of elements in $\{\Delta F_i/F\}$.

SI-9.5 Burst search

The burst search analysis complement the modulated signal analysis by focusing on the brief periods of high signal $\{\Delta F_i/F\}$ in a time-trace, instead of performing averages on the full time-trace. The motivation behind this type of analysis is to better discriminate the small, transient signal from the background under the assumption that pcNRs experience brief periods of transient insertion into/out of the membrane. Signal time-traces are reported in the notebook section 6 (link). The goal of burst search is detecting the time periods during which the fluorescent signal alternates in phase with the modulating voltage.

We start by computing the square of the running average of the $\{\Delta F_i/F\}$ signal using a block of 12 elements (*squared score*). When the squared score is higher than a threshold, a burst is detected. For each time-trace, the threshold was set to 60% of the maximum of the squared score. Next, for each burst *i*, we extracted the total signal (*burst score*)

$$S_i = \frac{1}{F}\sum_j \Delta F_j$$

Note that in the previous sum we have a minimum of 12 elements (j) that is the block size for the running average. However, depending on the signal, we can have longer bursts.

The quantity S_i represents the total amount of modulated signal present in each burst. In principle, the burst score can be either positive or negative, depending on whether the fluorescence intensity increases or decreases when the voltage is applied. For the pcNRs employed here, we find that the fluorescence is decreased (see fig. S10A). This is consistent with the observed excess of bursts with negative score for the selected particles on the patched cell membrane (see also main text).